MOUNTAIN-PLAINS CONSORTIUM

MPC 22-460 | C. Jiang, R. Atadero and P.R. Heyliger

AUTOMATING INSPECTION AND DAMAGE ASSESSMENT OF TRANSPORTATION INFRASTRUCTURE WITH STRUCTURE FROM MOTION

MOUNTAIN-PLAINS CONSORTIUM REGION 8

A University Transportation Center sponsored by the U.S. Department of Transportation serving the Mountain-Plains Region. Consortium members:

Colorado State University
North Dakota State University
South Dakota State University
University of Colorado Denver
University of Denver
University of Utah
Utah State University
University of Wyoming

Automating Inspection and Damage Assessment of Transportation Infrastructure with Structure from Motion

Chao Jiang
Rebecca Atadero
P.R. Heyliger

Department of Civil and Environmental Engineering
Colorado State University
Fort Collins CO 80523

June 2022

Disclaimer

The contents of this report reflect the views of the authors, who are responsible for the facts and the accuracy of the information presented. This document is disseminated under the sponsorship of the Department of Transportation, University Transportation Centers Program, in the interest of information exchange. The U.S. Government assumes no liability for the contents or use thereof.

Abstract

Several approaches are presented that allow for a direct path of image-to-analysis for the mechanics of structures using a combination of structure-from-motion (SFM) and the finite element method. Through these methods, conventional computational methods can be applied to models created from digital images of structures that may have been generated without conventional design methods. Several procedures are introduced to overcome limitations of SFM when applied to existing structural systems. Several models are used as means of demonstration for man-made structures, including a clock tower and several works of sculpture under both static and free vibration analysis.

TABLE OF CONTENTS

LIST OF TABLES

LIST OF FIGURES

1. INTRODUCTION

The application of new tools such as drones, scanners, and autonomous robots has allowed for far easier and more rapid means of data collection for a wide variety of uses. The use of these data has increasingly been applied to creating three-dimensional representations of spatial structures with levels of detail that are constantly improving. The physical systems to which these methods have been applied are diverse in terms of size, composition, and constitution and are not limited to civil *structures*. For example, Fantini et al. (2008) used imaging methods to reconstruct the missing part of a badly damaged medieval skull. Buck (2007) and his co-workers used 3D documentation methods to study the aftermath of a traffic accident. The 3D content derived from various sources has also been used to enrich cultural heritage digital libraries (CARARE 2018, 3D-ICONS 2019, 3D-COFORM 2019). Applications to a variety of structural systems is on the increase. There have been several software solutions based on the structure-from-motion (SFM) and dense multi-view 3D reconstruction (DMVR) algorithms that have been available in the past decade. By using unordered images of conventional digital photographs, these methods can generate high-quality 3D models that describe a scene or an object from a number of different views. The corresponding data evaluation using these methods has also increased in recent years. Koutsoudi (2014) and co-workers chose Greece as a study case to quantify the quality of a commercial SFM-DMVR software for a variety of uses. Lattanzi and Miller (2015) provided a comparison of two methods when reconstructing three-dimensional scenes for bridge inspection. Both of these studies achieved high-quality results that came with several caveats and warnings of limitations: 1) challenges based on the reliance on salient and robust local features, especially those sensitive to the lighting conditions, and 2) a loss of quality when a cluster of feature points was coplanar. They also indicated that these problems were obvious for a structure as simple as a clean steel plate. Since this material is common in many structures, the limitations could greatly restrict the application of this technique within the civil engineering field.

Conventional digital cameras have commonly been used to record photographic images during routine inspections to maintain a visual record of accumulated performance or appearance. However, this type of sensing is still somewhat of an intuitive method for most inspection methods based on visual observation (Hartle 2004). Computing advances have led to the increased use of robots as inspection tools (Devault 2000; Guo and co-workers 2009; Lim and co-workers 2011). Lubowiecka and co-workers (2009) used laser scanning and ground penetrating radar to study the health of a masonry structure. Park and co-workers (2007) proposed a procedure based on terrestrial laser scanning (TLS) for the measurement of deflections in bridges and buildings. Few studies have made the transition from SFM or TLS models directly to a computational platform for a full structural analysis of the system. Lattanzi and Miller (2015) have used this type of method for bridge inspection, and Conde-Carnero and co-workers (2016) transformed data from laser to finite element models for similar purposes. In the present study, several approaches are presented to connect a sequence of digital photographs with finite element models of the virtual structure that can be used for either static or dynamic analysis. By demonstrating the procedures that can be used to at least partially overcome some of the limitations associated with SFM, this provides a foundation of methodologies that can be adapted or perhaps combined using future developments.

2. METHODOLOGY

The analyses in this study are based on the combination of two tools: the transition of digital photographs to a finite element mesh, and the static or dynamic analysis of the system using standard finite element methods. In this section, the basic steps of each of these are described.

2.1 Mesh generation using SFM

In this section, the steps are discussed that allow the transformation from two-dimensional (2D) digital photos reconstructed from the real world into three-dimensional (3D) finite element models. In contrast to many techniques involving laser-based tools, SFM methods can directly build point clouds from photographic images disregarding the use of a transformation matrix (Conde-Carnaro and co-workers, 2016). Although specific elements of computational software were used for this particular study and are listed as a matter of completeness, the results could be generated by a number of alternative tools. There are two separate procedures outlined here, each of which can address some of the problems that can arise when transitioning from photographs to 3D idealizations but depend on the physical nature of the structure. There are several types of structures that more readily allow for the relatively straightforward generation of finite element models because the domains are relatively regular with smooth surfaces, lack gaps or voids, and are fairly homogeneous structures. There are others, however, that may be missing one or more of these basic features. In the examples that follow, a combination of both types of structure are considered to demonstrate some modifications and variations that may need to be introduced to generate accurate representations of the physical system.

2.1.1 The Isotropic Parallelepiped

As a simple initial example, a rectangular bar with a length of 160 mm, cross-sectional dimensions of 40 x 40 mm, and a mass of 580 grams was considered. The specimen dimensions have been computed to within 0.000254 meters and the mass to within 0.0001 grams. The elastic constants of this bar are known to be C_{11} = 21.86 GPa and C_{44} = 9 GPa. This is an extremely simple geometry but its natural frequencies have been determined using impact resonance methods (Heyliger and co-workers 2001) that can be compared with the SFM/FEM methodology discussed in this study.

A total of 96 digital images were used along with Photoscan, one of several commercial codes that use SFM techniques, to generate a point cloud representation of the parallelepiped whose dimensions in the three directions matched the values to within 0.0003 meters. In this case, the locations of the surface points had virtually no change and hence could all be assumed to be located along a planar surface. Hence, meshing for an object of this shape can almost be completed manually with any resolution necessary using standard methods since the six flat surfaces did not require any adjustment or special surface meshing. This solid was the only one considered in this study that allowed a direct comparison between theory and experiment for the computation of resonant frequencies. This is discussed in the next section.

In the remaining example structures, the geometries are far more complex, and a variety of methods were used to overcome some of the challenges associated with each specific structural system.

2.1.2 Dilitant Fault

Dilitant Fault is a metal man-made sculpture on the Colorado State University campus (Figure 2.1). A total of 366 digital photos were aligned to construct the complex geometry of the sculpture. When acquiring photos of this structure, the primary challenges were 1) inadequate color variation of the surface, and 2) corners and regions at the bottom of the sculpture were poorly lit under natural conditions because of the shading generated by the upper parts of the sculpture. However challenging, these conditions were not uncommon and provided a useful case on which to attempt direct modeling.

Since the color of the sculpture was not completely monochrome, even the slight change of color and pattern on the surface helped with the alignment of the photos. Several photos were aligned incorrectly during the first attempt at cloud generation. The sparse points associated with these photos can be easily seen in the sparse point cloud view shown in Figure 2.1. In a subsequent attempt, more photos were aligned correctly, and a reasonable 3D surface model was successfully constructed and converted into a compatible FE model in Abaqus CAE. This mesh is also shown in Figure 2.1.

Repair of non-manifold 3D models after the initial construction of the 3D model is important because it will directly affect whether or not the model is able to be analyzed using FEM software packages. Autodesk NetFabb, an additive manufacturing and design software that supports automatic repair solution for non-manifold 3D models, was used to resolve the issues with holes and self-intersection in the 3D surface model of this structure. It is common that some of the individual surfaces in the generated model can be too close to each other, which prevents the direct conversion to a 3D solid. In this case, other tools (Rhino) can be used to provide additional adjustments to ensure that the polysurface model is valid and manifold, allowing the transformation from the 3D surface to a 3D solid.

2.1.3 Clock Tower

Some structures admit meshing choices that depend on the level of detail sought by the analyst. Figure 2.2 shows the point cloud of a solid masonry clock tower on the campus of Colorado State University. At one level, this system somewhat resembles the rectangular bar examined in the prior section. Yet, here the nature of construction provides a far more complex surface than the uniform metal plane and provides an array of choices that depend on what sort of behavior is being monitored.

The point cloud in Figure 2.2 was generated using a total of 251 digital images. SFM methods rely on local features of the structure for the creation of the point cloud, and the result shown in this figure allows for an excellent reproduction of the actual physical structure. In order to transition from the point cloud to an effective finite element model, there are several problems that can arise and must be addressed. The first is the possibility of redundant points in the point cloud. For the clock tower, the points associated with the vegetation at the base of the structure serve as examples. These points can be removed by saving the point cloud as an .obj file and using editing software that not only removes the redundant points but also reduces the number of so-called noisy points. A second issue is the potential gaps in the point cloud that can arise from a number of issues, including but not limited to an inadequate number of digital photographs or

poor lighting. In this case, it is frequently possible to interpolate missing points in the data based on the location of existing points, thus generating a continuous surface that is representative of the point cloud geometry. In this example, both of these challenges were resolved using the software 3DReshaper (2016) with the resulting surface representation shown in Figure .2.3. This is not the mesh used for final analysis but was required to develop such a model.

The present method of analysis requires transfer from the surface mesh shown in Figure 2.3 to a volume mesh that represents the domain within the solid. This mesh must embed the ability to adjust any global coordinate systems to ensure that, for example, gravity loads are always acting in physically meaningful directions. Several computational tools have difficulty generating appropriate meshes using only surface data. In this study, .stl or .igs files were generated from 3DReshaper and imported to Truegrid (2006), a tool that can effectively build volume meshes from surface data without having to use an excessive number of elements. This process was used to generate a mesh of 9850 3D elements, most of which were hexahedral as shown in Figure 2.4. Such a mesh could be imported to any standard finite element software. The analysis of such a system is discussed in a later section.

2.1.4 Shoulders of Giants

The level of difficulty in generating finite element models from photographic images can increase when gaps, voids, and elements with varying aspect ratios are present. Some adjustments to the process may be necessary in such cases. As a model problem, the sculpture Shoulders of Giants at Colorado State University, shown in Figure 2.5, was used.

Using similar procedures as those used for the clock tower in the previous section, 333 photos were used to generate the point cloud shown in Figure 2.6. Because of the size of this structure, both ground-based and drone-based photos were used. A direct comparison of this point cloud with that from the clock tower indicates a drastic drop in relative quality, and a direct transition to a surface mesh, would yield poor results. Although more digital images would improve the quality of the point cloud, it is useful to explore alternatives that may provide sufficient accuracy.

The drop in quality of the point cloud is induced by several factors. First, because of the nature of the material that comprises this system (metallic versus masonry), the reflection of surface light initiates challenges for the imaging software to distinguish between the relative color of adjacent data points. Second, SFM software depends on the salient local features for creation of the point cloud. Images taken from relatively large distances, including those taken by drone based on requirements of maintaining an adequate distance between the structure and the drone camera, can lead to the loss of local data points. Finally, when the structural elements are relatively thin, it can be difficult for the SFM software to distinguish between points on the same surface versus those that may be located on the opposite side of the structural element. This is because meshing tools are based on the locations of neighboring points within the point cloud, and points that may appear to exist on the same surface from one view can in fact be on different surfaces when more images are used.

In an attempt to overcome these limitations without requiring a massive increase in the number of digital images used, an alternative methodology was employed. The general idea was to reduce the number of points that generated geometric ambiguity by deleting relatively noisy or geometrically variable points by exporting the point cloud into an .obj file and importing these data to software, such as 3DReshaper, for the purpose of editing and interpolating points that are both geometrically admissible and consistent with the actual geometry. The refined point cloud generated following such a step is shown in Figure 2.7 and is a clear improvement over the initial point cloud.

Following the creation of the refined point cloud, virtually all ambiguous points have been removed and the generation of a solid model using tools such as Rhino is relatively straightforward. Using features such as cutting plates, extensions, and solid cutting, the solid system can be reconstructed as shown in Figure 2.8. In this case, however, this model is a solid rather than a surface that was generated from the approach used in the clock tower. Before directly importing this solid into finite element software, several intermediate steps are required.

First, the model needs to be geometrically dissected into sub-domains with regular geometry. This is because some finite element meshing software lack the capability to detect the basic features of the system geometry. This is especially true for the thin elements in the structure, where tools such as Truegrid can generate meshing errors during projection. It is also typical to generate overlapping regions within drawings that can cause overlapping regions of meshing. However, tools such as Rhino allow for Boolean operation segmentation, which aims at cutting the model into pieces using nearby surfaces. Second, because of the imperfect drawings that can be generated in Rhino, some parts contain superfluous lines that can affect the mesh type and need to be removed. In addition, the surfaces that will either connect the subdomains or form the actual external boundary of the solid need to be defined. Once these tasks are completed, the volume mesh of the solid follows in a straightforward fashion, with the resulting reconstruction shown in Figure 2.9.

2.2 Finite Element Analysis

All example problems considered here can be assumed to respond according to the assumptions and governing equations of 3D linear elasticity. This is a very well-studied problem and only the broad outline of the solution procedure is discussed here. General finite methods give the approximate solution of Hamilton's Principle.

The core of the finite element method is to seek the approximate solution with respect to displacement components, which can be given as the following forms:

$$u_i = \sum N_j^u \varphi_j(x_i)$$

Here j is the nodal value of each displacement and $\varphi_j(x_i)$ are the corresponding approximation functions.

For a solid, which is conformed to the constitutive law, the stress components can be founded in displacement field. And the deformation is the sum of each displacement while the external loads act on the solid (Zienkiewicz 2013, Reddy 2006, Thompson 2004).

3. RESULTS AND DISCUSSION

In this section, the results from the finite element analysis are presented for the representative test cases whose meshes were developed using SFM techniques. The results include displacement and stress field estimates under gravity and wind loads and free vibration response of the structure. These results are grouped according to the specific structures considered above.

3.1 Isotropic Parallelepiped

The resonant frequencies of the isotropic parallelepiped were computed for this structure using a relatively fine mesh of 32,000 8-noded brick elements using the mesh determined from the SFM procedure. The type of mode can be identified from modal displacement patterns. Three of the primary modes of vibration can be excited using impact resonance \cite{kn:heyligerugander}, in which part of the structure is struck with a small hammer to excite one of the modes of vibration. The longitudinal, twisting, and bending frequencies of this specimen can be determined in this fashion by striking the parallelepiped on the end face in the long direction of the specimen, at one of the corners in the direction of either of the small dimensions of the cross-section, and at the mid-point of the long dimension in a direction perpendicular to the long dimension of the specimen, respectively. The results of the finite element analysis are compared to the experimental results and those of the Ritz method in Table 3.1, with excellent agreement being found.

Table 3.1 Frequencies (Hz) for the isotropic parallelepiped

Method	Flexural	Longitudinal	Torsional
Experiment	4320	9434	5731
Ritz	4334	9435	5731
Present	4336	9438	5733

3.2 Dilitant Fault

Because of the nature of this structure in terms of its unusual geometry, the influence of mesh convergence was examined in detail for two parameters: the first 10 frequencies of natural vibration and the peak displacement and von Mises stress under the application of a point load of 750 N at the top peak of the solid. This load was meant to represent that induced by a typical human standing on top of the sculpture. Three different meshes were considered using the methodologies described in the previous section. Using these discretizations, both the free vibration analysis and static response were computed as a function of mesh size. In all cases, the material properties were taken to be that of steel, with an elastic modulus of 200 GPa, a Poisson ratio of 0.3, and a density of 8050 kg/m^3.

The results of this analysis are shown in Table 3.2 for the displacement/von Mises stress calculations and Table 3.3 for the natural frequencies. Aside from the coarsest mesh used of 7,726 elements, the results for all remaining meshes are quite consistent for all parameters measured. The results also indicate there is a factor of safety of at least 15 when it comes to concerns about loading the structure to the point of failure. On other words, it would take well over 15 people standing on the sculpture peak to potentially initiate yielding. While unlikely,

there are in fact rather fragile structures—both natural and manufactured -which are subjected to loadings that may not possess such robust residual strength. This methodology would allow estimates to be obtained where the geometric domain can be found to within very small error tolerances.

Table 3.2 The maximum displacement and von Mises stress as a function of the number of elements N for Dilitant Fault

N	Displacement (m)	Peak Stress (MPa)
7726	1.997×10^{-3}	17.8
24860	1.862×10^{-3}	26.0
58458	1.861×10^{-3}	26.4

Table 3.3 The first 10 natural frequencies as a function of the number of elements N for Dilitant Fault

N	Mode									
	1	2	3	4	5	6	7	8	9	10
7726	9.96	12.72	17.97	22.34	35.39	40.99	54.04	56.81	88.98	93.61
24860	9.65	12.91	17.26	20.83	34.57	40.60	52.73	54.36	84.90	88.65
58458	9.69	12.83	16.68	20.59	33.70	40.28	50.87	54.14	83.12	86.28

3.3 Clock Tower

The material properties used for the clock tower are representative of the sandstone blocks used to build the structure with an elastic modulus of 6.9 GPa, a Poisson ratio of 0.25, and a density of 1922 kg/m^3. Two different analyses were completed: the static response under gravitational and wind loading, and the free vibration response. The wind load was treated as a transverse pressure that acts perpendicular to the tower faces with a peak of 100 Pa. The boundary conditions and loads on the finite element model are shown in Figure 3.1. Using both imaging and physical measurements, the dimensions of the tower were 1.61 meters wide, 0.40 meters thick, and 3.61 meters tall. Following the image processing, a mesh with 3,190 nodes and 2,344 elements was used to obtain the results that follow after a convergence study.

The transverse deflection and von Mises contours are shown in Figures 3.2 and 3.3, respectively. These indicate regions dominated by rigid body motion for much of the upper section of the tower under this type of loading. The contours are not perfectly symmetric across the width of the tower, which is indicative of both slight geometric deviations from symmetry in the actual tower and slight errors induced by the imaging process. Yet, the overall response contains much of the structural symmetry.

The first 10 frequencies of natural vibration are shown in Table 3.4, with the corresponding mode shapes shown in Figure 3.4. There are few surprises in terms of frequency order, with the first three modes describing bending, axial, and twisting motion. It is notable that the bending frequencies for a Euler-Bernoulli beam under the clamped-free conditions that are similar to those of the clock tower are given by

$$\omega_n = (\beta_n L)^2 \sqrt{\frac{EI}{\rho A L^4}}$$

Here ω_n is the n-th natural frequency in radians/second, E is the modulus of elasticity, I is the second moment of the cross-sectional area about the section centroid, A is the cross-sectional area of the section, and L is the beam length. The roots β_n are solved using the equations of motion, with the first four values given as 1.8751, 4.6941, 7.8547, and 10.9956. This indicates that the ratios of the bending modes to their next modes are 0.16, 0.36, and 0.51 for the first four modes. The results of the solid clock tower are 0.18, 0.39, and 0.57 for the bending modes 1, 4, 8, and 10. This is not to argue that the clock tower can be represented by a one-dimensional shear-free beam, but the primary bending modes appear to possess that character.

Table 3.4 The first 10 frequencies of the clock tower (Hz)

Mode	Frequency
1	9.70
2	32.3
3	40.8
4	55.7
5	124
6	130
7	133
8	147
9	222
10	260

3.4 Shoulders of Giants

The material properties used for the analysis of the Shoulders of Giants sculpture were an elastic modulus of 210 GPa, a Poisson ratio of 0.3, and a density of 7,800 kg/m^3. For this geometry, only the free vibration response was considered. The geometry and boundary conditions are shown in Figure 3.5. The first 10 frequencies are shown in Table 3.5. It is clear that for this structure the vibrational modes are dominated by larger deflections in the more slender sections of the structure. The frequencies are lower, by an order of magnitude, than those for the clock tower. This is expected because this structure has much lower relative stiffness than the short, stubby geometrical configuration of the clock tower.

Table 3.5 The first 10 frequencies (Hz) under free vibration for Shoulders of Giants

Mode	Frequency
1	0.8854
2	0.9726
3	1.1038
4	1.1246
5	1.3162
6	1.4241
7	1.6776
8	3.4962
9	4.0651
10	4.6002

4. SUMMARY

Based on different geometries, this study provides background and examples of methodologies to apply SFM construction of models from 2D digital photographs for finite element analysis. An array of structures was chosen to illustrate these methodologies and show methods to overcome the limitations of SFM when applying these approaches to challenging geometries. Results of representative problems were presented to give examples of actual numerical calculations for stress fields and vibrational modes for structures composed of metals, wood, and masonry. To the authors' knowledge, there are few if any applications of SFM approaches and finite element results in the literature, and these initial studies provide a glimpse of what might be accomplished with more refinement and study.

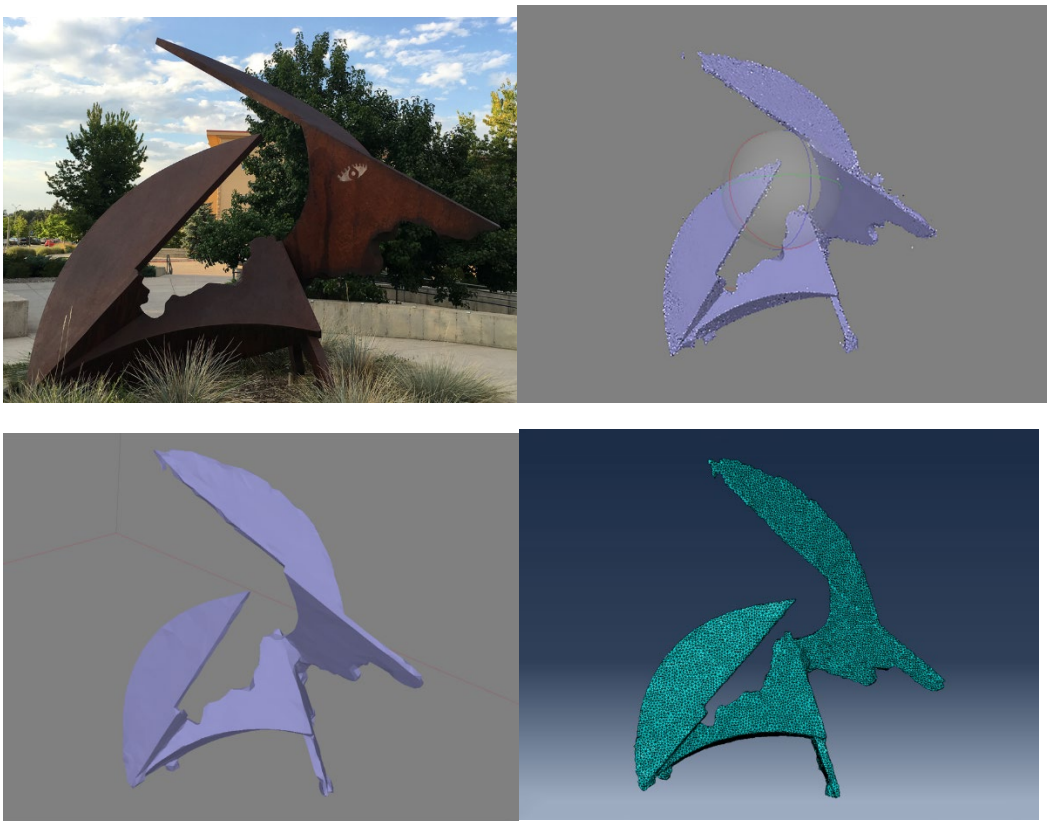

Figure 2.1 The Dilitant Fault sculpture on the campus of Colorado State University

Figure 2.2 The point cloud of clock tower generated by Photoscan

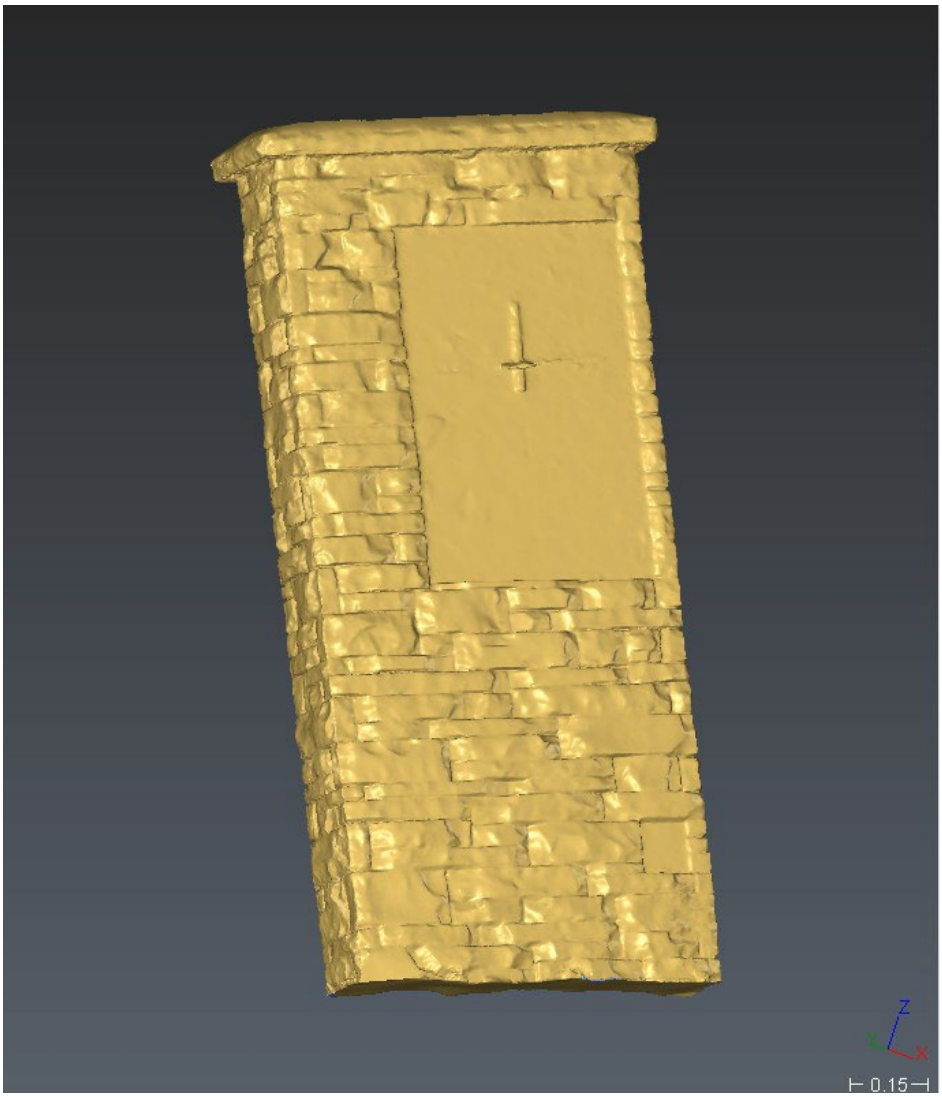

Figure 2.3 The surface mesh created by 3DReshaper

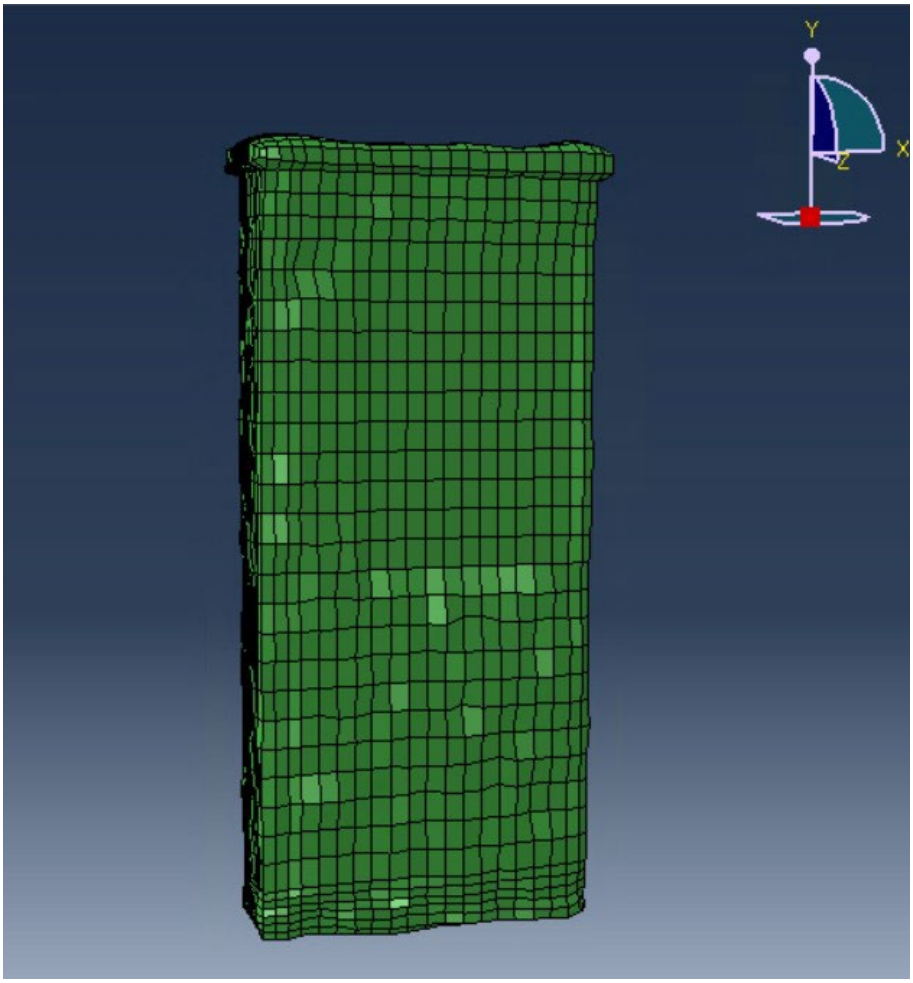

Figure 2.4 The volume mesh of clock tower created by Truegrid

Figure 2.5 Shoulders of Giants sculpture

Figure 2.6 The point cloud of the shoulder generated by Photoscan

Figure 2.7 The refined point cloud by using 3DReshaper

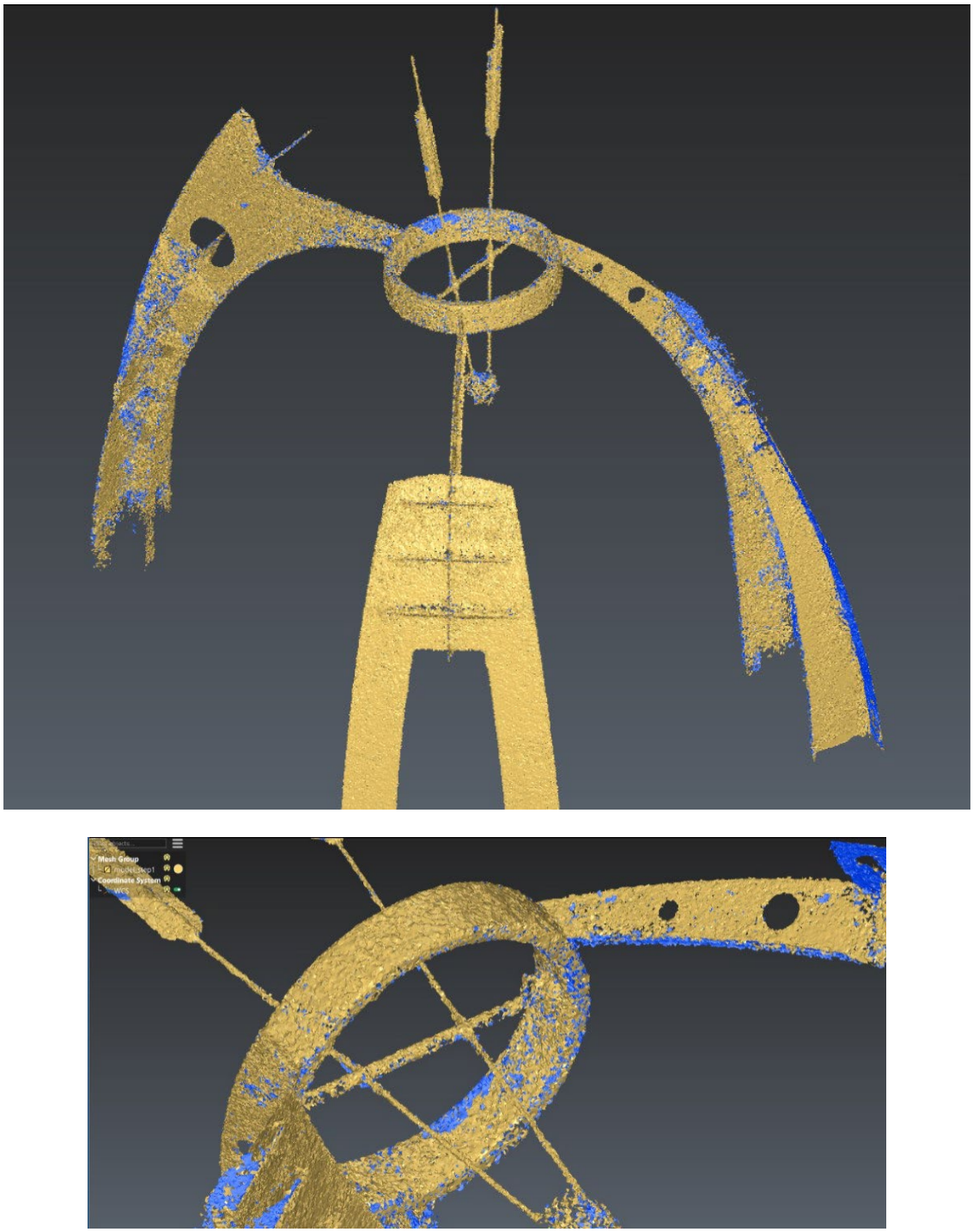

Figure 2.8 The mesh formed using 3DReshaper

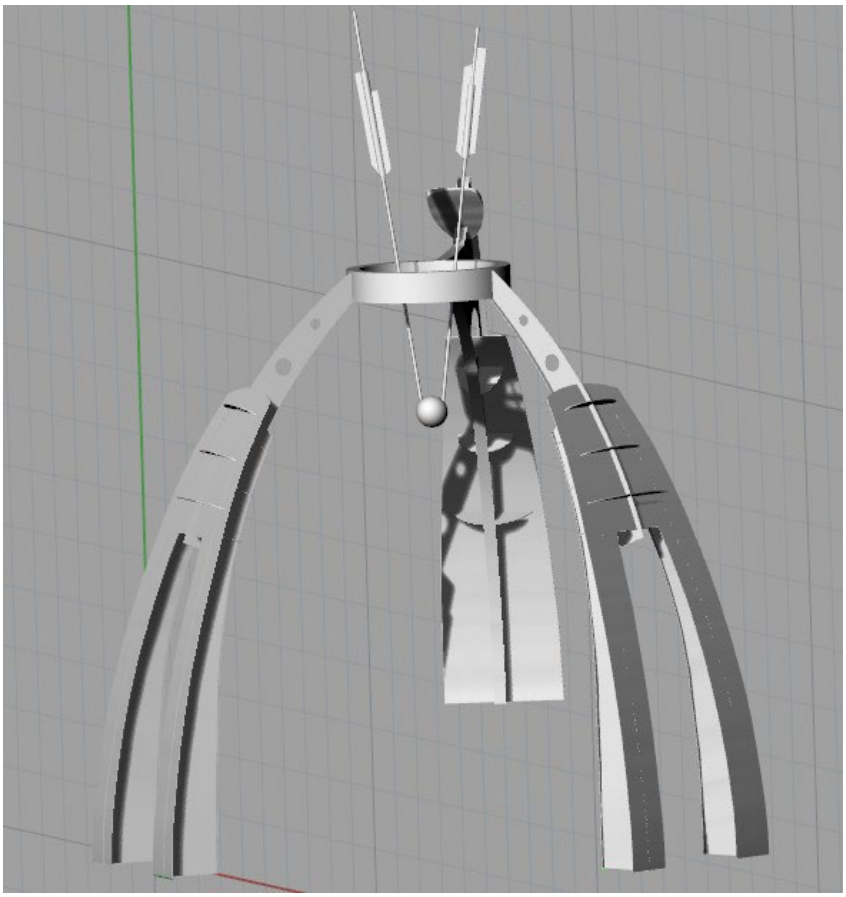

Figure 2.9 Shoulders of Giants after reconstruction in Rhino

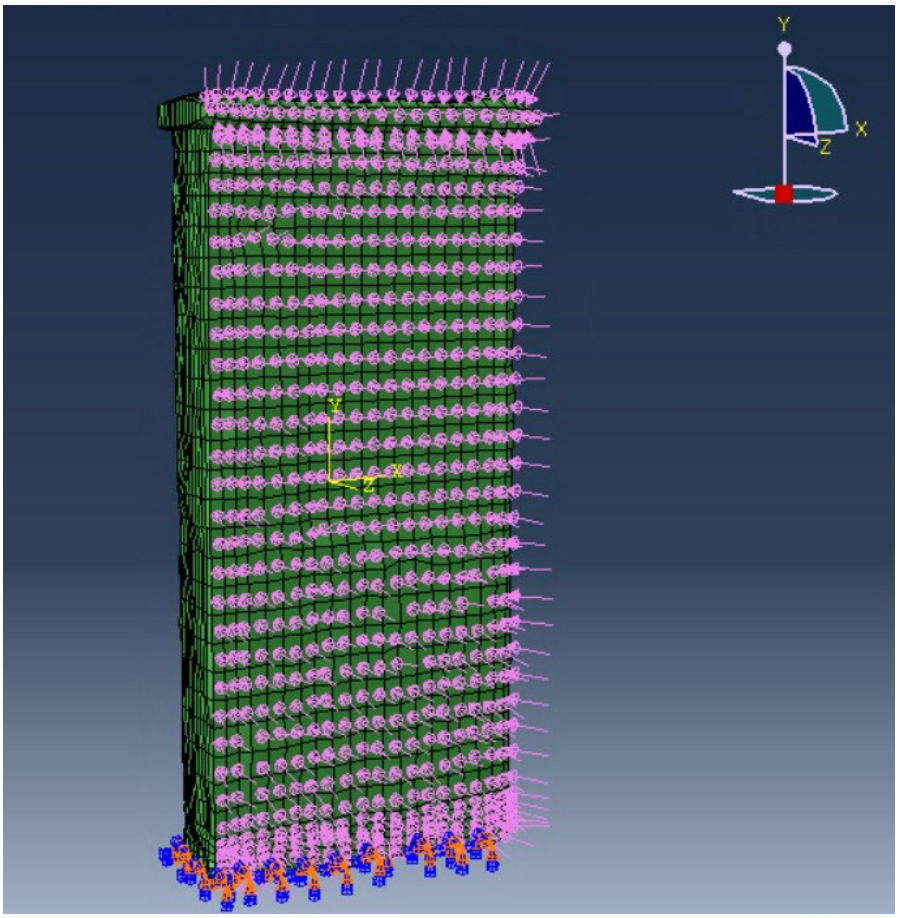

Figure 3.1 Model with boundary conditions under wind and gravity loads

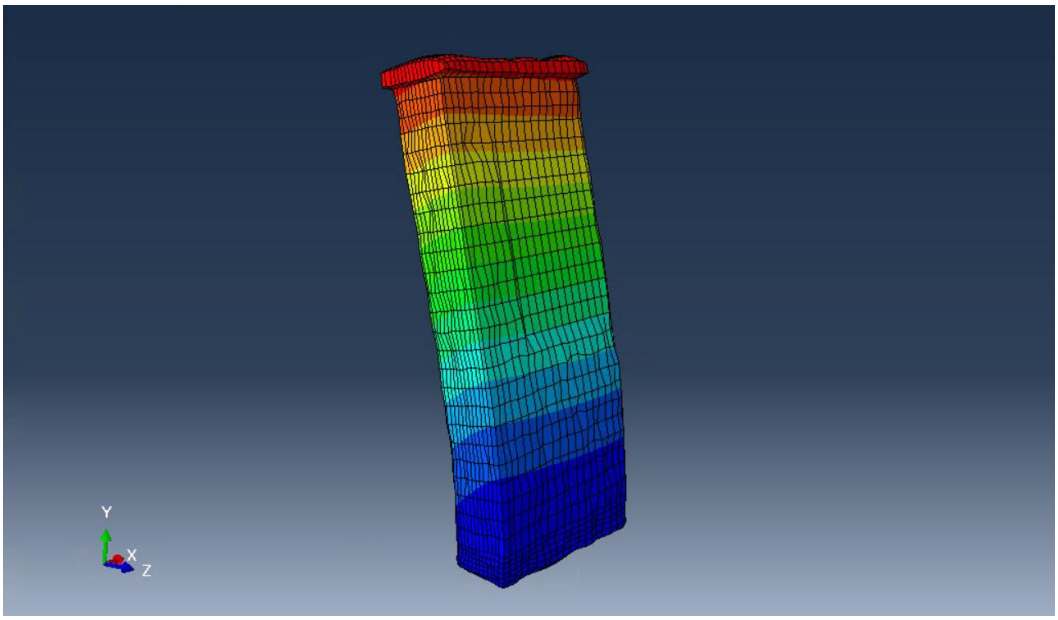

Figure 3.2 The deflection of clock tower under gravity and wind loads

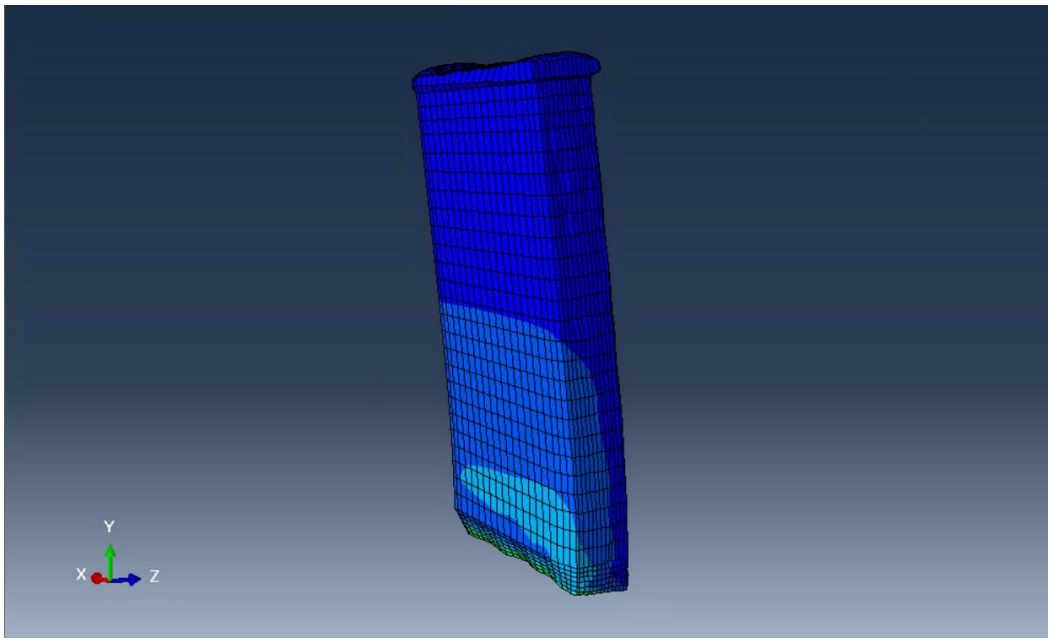

Figure 3.3 The Von Mises stress distribution of clock tower under gravity and wind loads

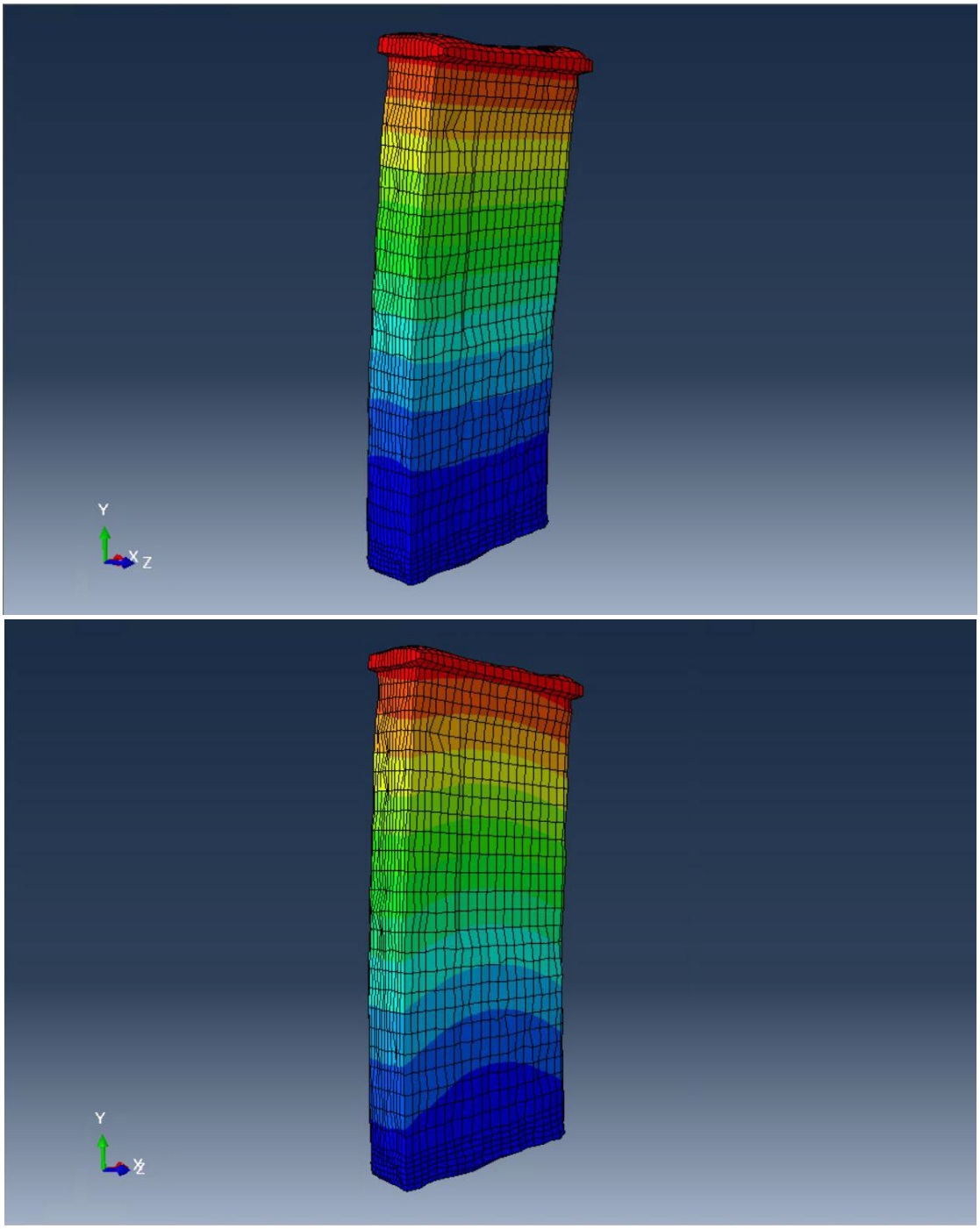

Figure 3.4 First 10 vibrational modes of the clock tower

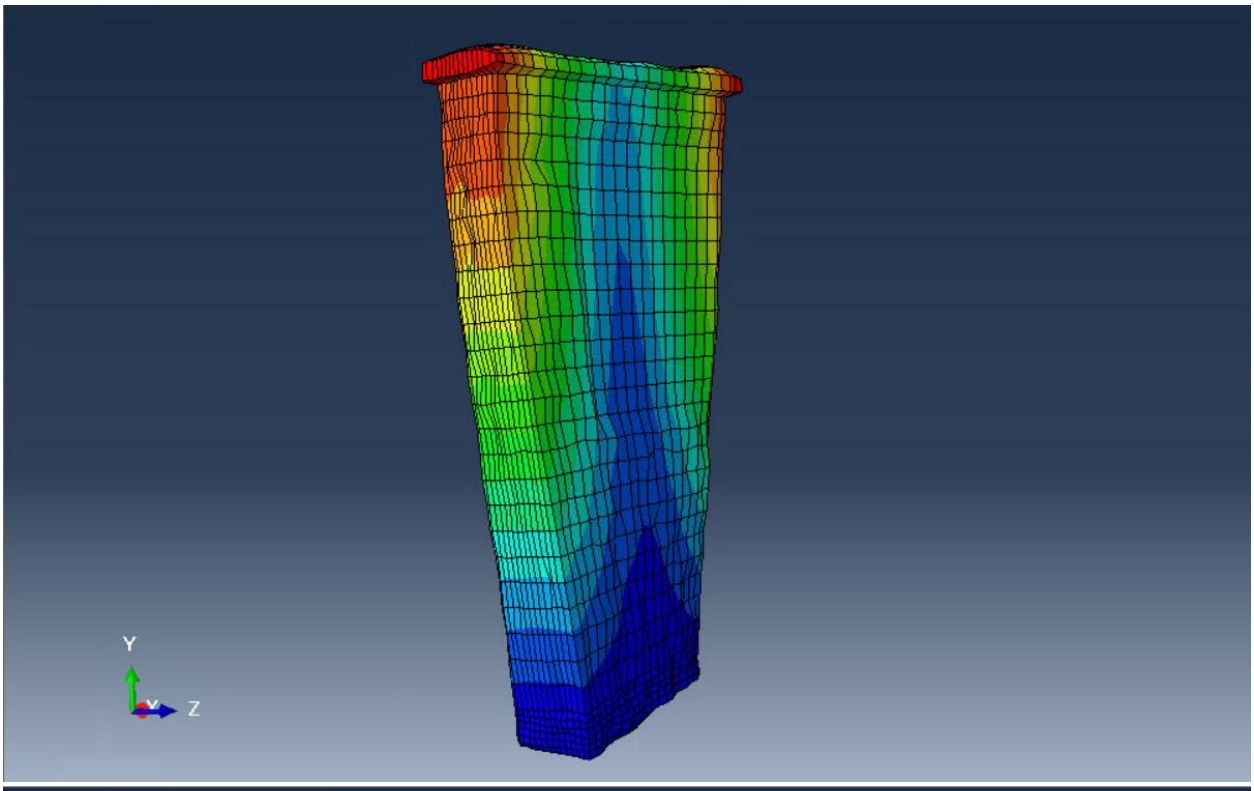
Y
Z

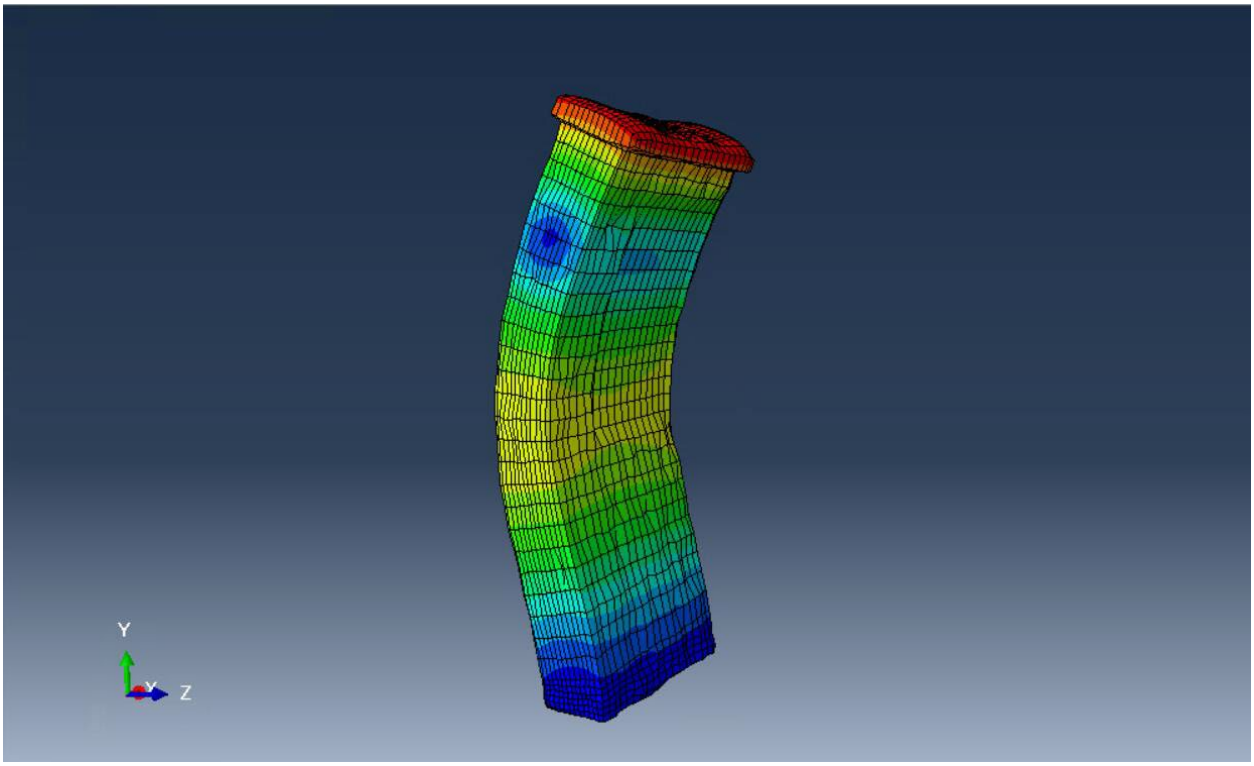
Y
Z

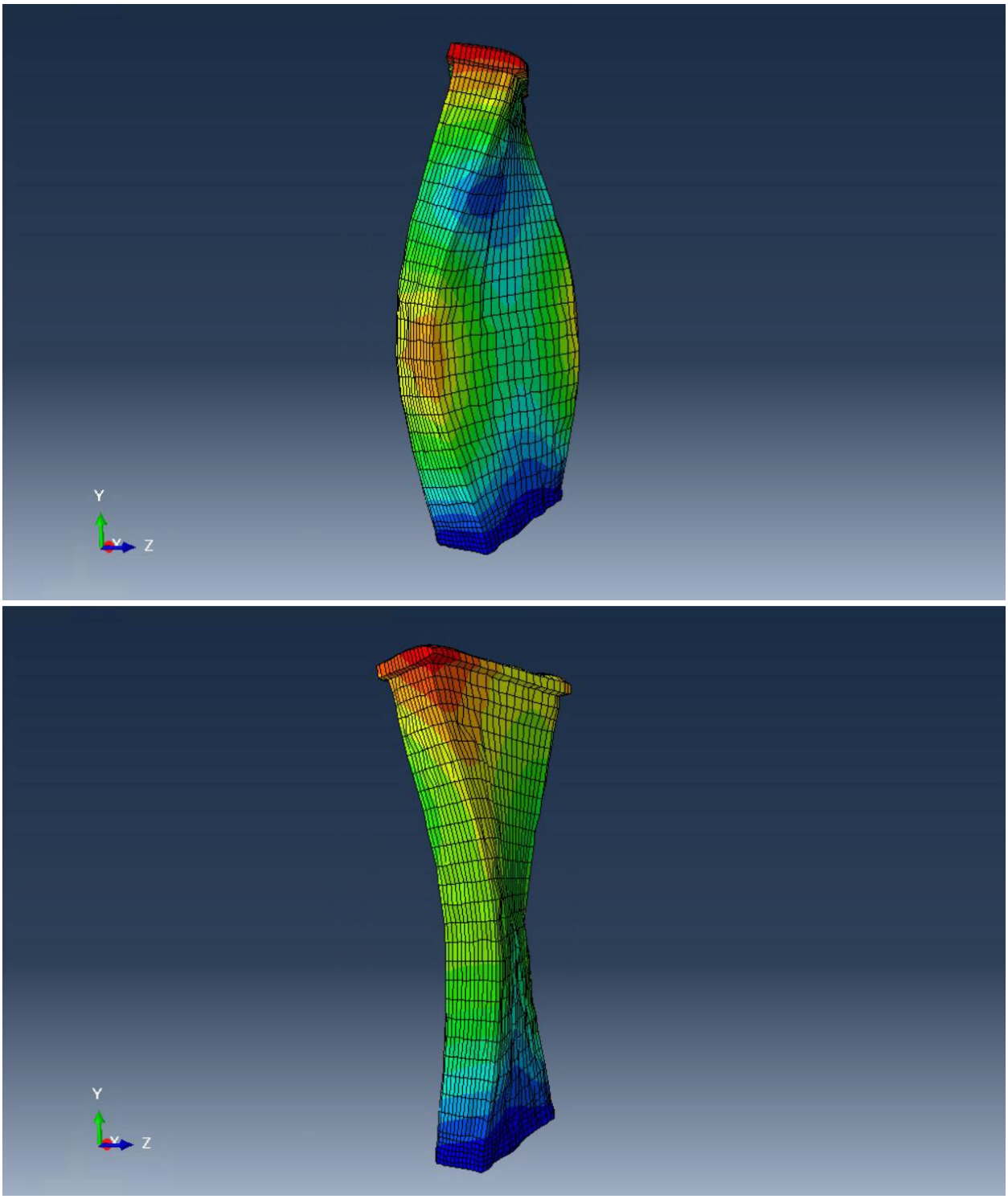
Y
Z
Y
Z

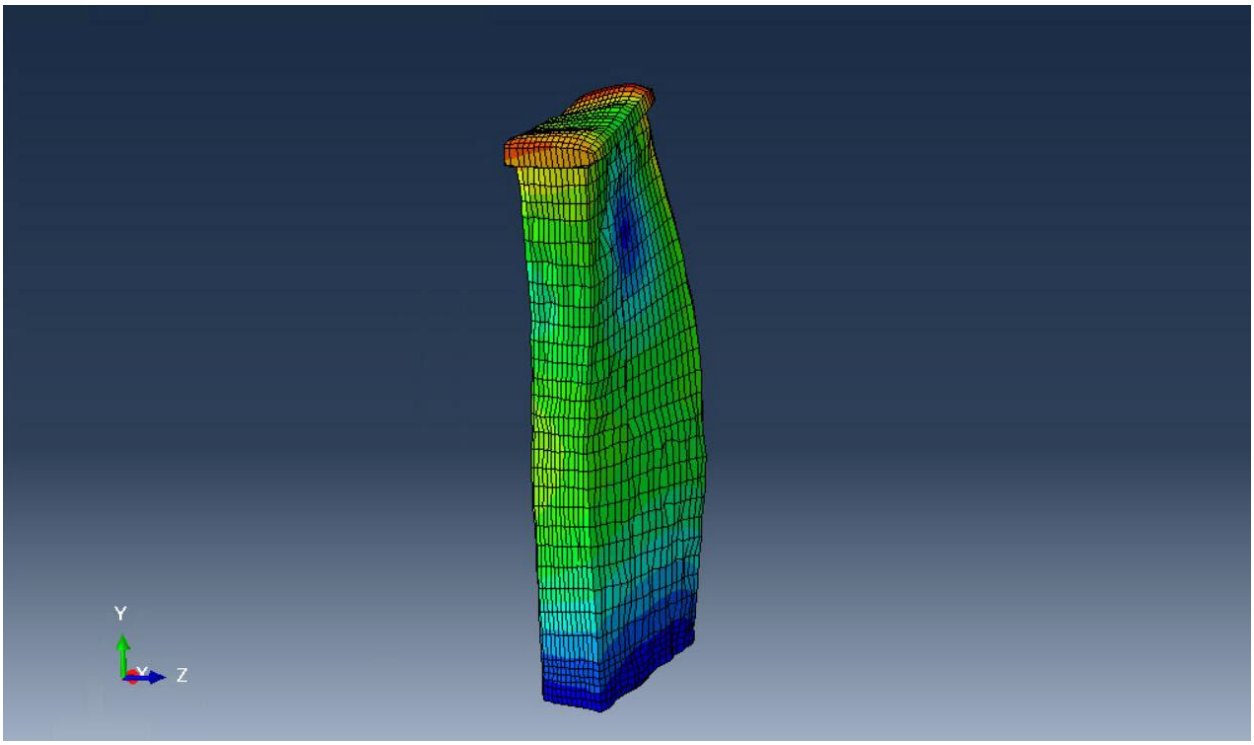
Y
Z

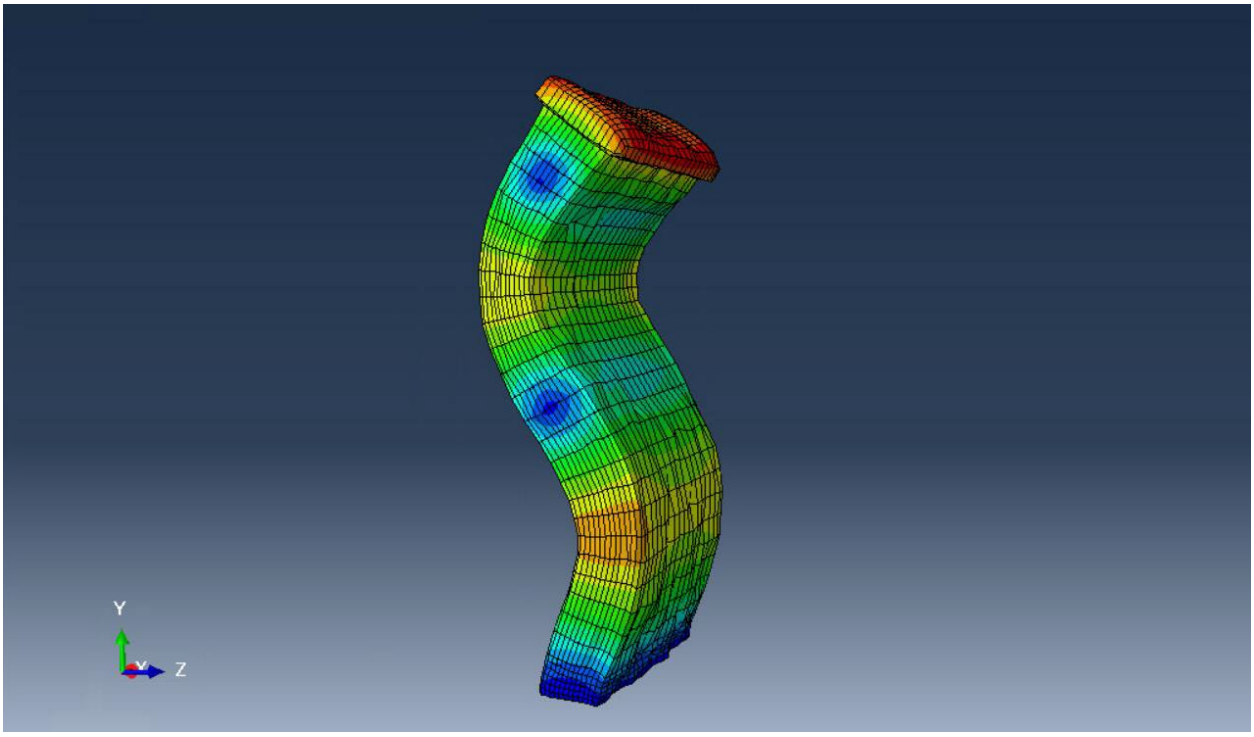
Y
Z

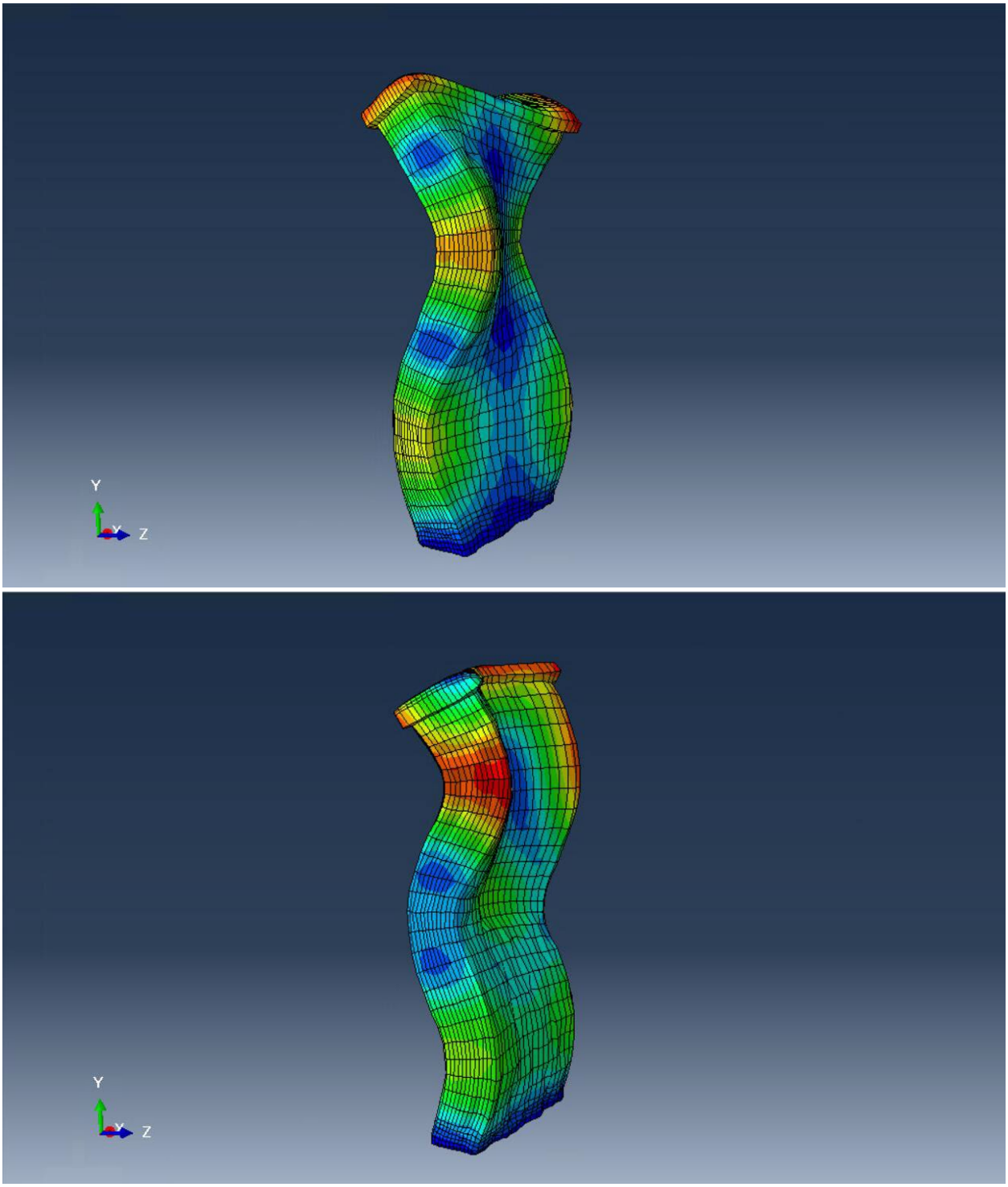
Y
Z
Y
Z

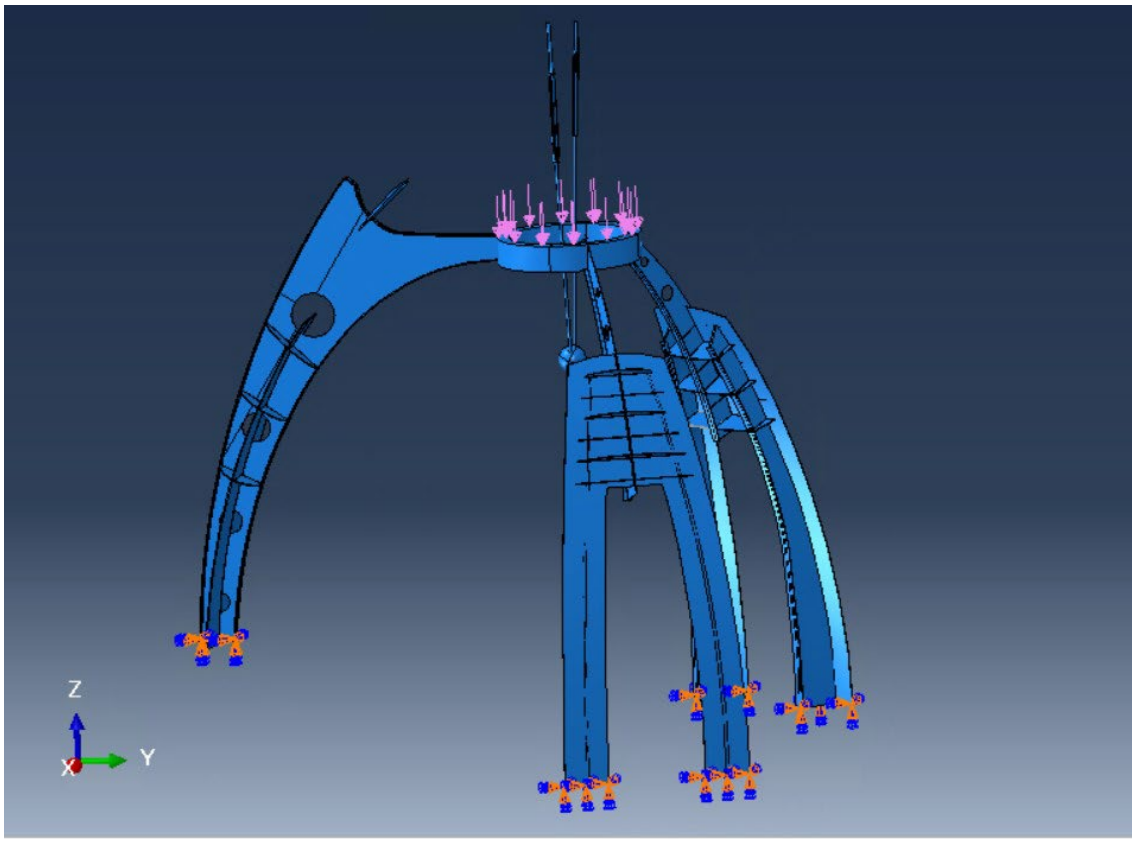

Figure 3.5 The model after applying loads and boundary conditions

REFERENCES

[1] Fantini, M. (2008), "3D Restitution, Restoration and Prototyping of a Medieval Damaged Skull," *Rapid Prototyping Journal*, 14(5), 318-324.

[2] Buck, U., Naether, S., Braun, M., Bolliger, S., Friederich, H., Jackowski, C., Aghayev, E., Christe, A., Vock, P., Dirnhofer, R., & Thali, M. J. (2007), "Application of 3D Documentation and Geometric Reconstruction Methods in Traffic Accident Analysis: With High Resolution Surface Scanning, Radiological MSCT/MRI Scanning and Real Data Based Animation," *Forensic Science International,* 170(1), 20-28.

[3] CARARE Best Practice Network (2018), http://www.carare.eu.

[4] 3D-ICONS pilot project, http://3dicons-project.eu.

[5] 3D-COFORM. consortium, http://3dcoform.eu.

[6] Koutsoudi, A., Vidmar, B., Ioannakis, G., Arnaoutogloua, F., Pavlidis, G., & Chamzas, C. (2014), "Multi-image 3D Reconstruction Data Evaluation," *Journal of Cultural Heritage*, 15(1), 73-79.

[7] Lattanzi, D., & Miller, G. R. (2015), "3D Scene Reconstruction for Robotic Bridge Inspection," *Journal of Infrastructure Systems*, 21(2), 04014041.

[8] Hartle, R. A., & Administration, F. H. (2004), Bridge inspectors reference manual, U.S. Dept. of Transportation, Washington DC.

[9] DeVault, J. E. (2000), "Robotic system for underwater inspection of bridge piers," *IEEE Instrumentation & Measurement Magazine*, 3(3), 32-37.

[10] Guo, W., Soibelman, L., & Garrett Jr, J. H. (2009), "Automated defect detection for sewer pipeline inspection and condition assessment," *Automation in Construction*, 18(5),587{596.

[11] Lim, R. S., La, H. M., Shan, Z., & Sheng, W. (2011), "Developing a crack inspection robot for bridge maintenance," IEEE International Conference on Robotics and Automation, 6288-6239.

[12] Lubowiecka, I., Armesto, J., Arias, P., & Lorenzo, H. (2009), "Historic bridge modelling using laser scanning, ground penetrating radar and finite element methods in the context of structural dynamics," *Engineering Structures*, 31(11), 2667-2676.

[13] Park, H. S., Lee, H. M., Adeli, H., & Lee, I. (2007), "A new approach for health monitoring of structures: Terrestrial laser scanning," *Computer-Aided Civil and Infrastructure Engineering*, 22(1), 19-30.

[14] Westoby, M. J., Brasington, J., Glasser, N. F., Hambrey, M. J., & Reynolds, J. M. (2012), "Structure-from-Motion photogrammetry: A low-cost, effective tool for geoscience applications," *Geomorphology*, 179(15), 300-314.

[15] Conde-Carnero, B., Riveiro, B., Arias, P., & Caamano, J. C. (2016), "Exploitation of Geometric Data provided by Laser Scanning to Create FEM Structural Models of Bridges," *Journal of Performance of Constructed Facilities*, 30(3), 04015053.

[16] Zienkiewicz, O. C., Taylor, R. L., & Zhu, J. Z. (2013), *The Finite Element Method: Its Basis and Fundamentals*, 7th Edition, Butterworth-Heinemann, Oxford UK.

[17] Reddy, J. N. (2006). *An Introduction to the Finite Element Method*, 3rd Edition, McGraw-Hill, New York .

[18] Thompson, E. G. (2004). *Introduction to the Finite Element Method: Theory, Programming, and Applications*, Wiley, New Jersey.

[19] 3DReshaper MR1-Beginner's Guide (2016), http://www.3dreshaper.com/en/software-en/download-software/brochures-and-technical-documents

[20] Truegrid (2006), http://www.truegrid.com/pub/TGMAN230.1.pdf

[21] Truegrid (2006), http://www.truegrid.com/pub/TGMAN230.2.pdf

[22] Abaqus, http://www.3ds.com/productsservices/simulia/products/abaqus.

[23] Heyliger, P. R., Ugander, P., and Ledbetter, H. (2001), "Anisotropic Elastic Constants: Measurement by Impact Resonance," *ASCE Journal of Materials in Civil Engineering*, 13, 356-363.